arXiv:1601.08225v2 [quant-ph] 9 Dec 2016

Twisted Interferometry: the topological perspective

Parsa Bonderson [a], Lukasz Fidkowski [a], Michael Freedman [a,b], Kevin Walker [a]

[a] *Station Q, Microsoft Research, Santa Barbara, California 93106-6105, USA*

[b] *Department of Mathematics, University of California, Santa Barbara, California 93106, USA*

Abstract

Three manifold topology is used to analyze the effect of anyonic interferometers in which the probe anyons' path along an arm crosses itself, leading to a "twisted" or braided space-time trajectory for the probe anyons. In the case of Ising non-Abelian anyons, twisted interferometry is shown to be able to generate a topologically protected $\pi/8$-phase gate, which cannot be generated from quasiparticle braiding.

Key words: Interferometry; Anyonic charge measurement; Topological quantum computation.
PACS: 03.67.Lx, 03.65.Vf, 03.67.Pp, 05.30.Pr

1 Introduction

Anyonic interferometry [1,2] is a powerful tool for processing topological quantum information [3,4,5,6,7,8,9]. Its ability to non-demolitionally measure the collective anyonic charge of a group of (non-Abelian) anyons, without decohering their internal state, allows it to generate braid operators [10,11], generate entangling gates [12,13,14,15], and change between different qubit encodings [14,15]. Anyonic interferometry has been the focus of myriad experimental proposals [16,17,18,19,20,21,22,23,24,25,2
and efforts to physically implement them [30,31,32,33,34,35,36]. As powerful as anyonic interferometry may be, its potential capabilities have yet to be fully understood. In this paper, we propose and analyze a novel implementation of anyonic interferometry that we call "twisted interferometry," which can significantly augment its potential capabilities.

One of the primary practical motivations for studying twisted interferometry is that it could be used with anyons of the Ising TQFT to generate "magic states," as we will demonstrate. This is significant because, if one only has the ability to perform

braiding operations and *untwisted* anyonic interferometry measurements for Ising anyons, then one can only generate the Clifford group operations, which is not computationally universal and, in fact, can be efficiently simulated on a classical computer [37]. However, if one supplements these operations with magic states, then one can also generate $\pi/8$-phase gates, which results in a computationally universal gate set [38].

The application of twisted interferometry to generating the $\pi/8$-phase gate for Ising anyons is the latest link in a chain of ideas [39,40,41,42], originating with the unpublished work of Bravyi and Kitaev, for generating a topologically-protected computational universal gate set from the Ising TQFT by utilizing topological operations. The concept and analysis of twisted interferometry is new, but closely connected to these ideas, which stem from the concept of Dehn surgery on 3-manifolds. As we will discuss in detail, anyonic interferometry: 1) projectively measures the topological charge inside γ, and 2) decoheres the anyonic entanglement between the subsystems inside and outside the interference loop γ [43]. Both operations have a 3D topological interpretation in the context of Chern-Simons theory or, more generally, axiomatic (2+1)D topological quantum field theories (TQFTs). We learned from Witten [44] that all low energy properties of systems governed by a TQFT can be calculated in a Euclidean signature diagrammatic formalism called unitary modular tensor categories (UMTC). This suggests [40,41] that the choice of interference loop γ should not be restricted to a simple space-like loop in a spatial slice $\mathbb{R}^2 \subset \mathbb{R}^2 \times$time, as is the typical design for an interferometer, but rather γ might be a general simple closed curve of space-time. Twisted interferometry explores this direction by allowing the probe anyons' path through the arms of the interferometer to be self-crossing in $\mathbb{R}^2$ (so γ is *immersed* in mathematical terminology). We give a general procedure for analyzing interferometers of this kind. In the restricted case of the Ising TQFT, we describe a twisted interferometer which would be capable of producing magic states.

Our strategy is: 1) to start with the UMTC calculation [1,2] which lays bare the asymptotic behavior of the simplest anyonic Mach-Zehnder interferometer (and serves as a model for Fabrey-Pérot type interferometers in the weak tunneling limit); 2) describe this behavior in an equivalent topological language; and 3) exploit the general covariance inherent in the topological description.

The concrete calculation using the machinery of UMTCs is carried out in a companion paper [45], which also focuses on possible physical implementations of twisted interferometers. The analysis of the companion paper agrees with the topological argument presented here and both show how magic state production is achieved when specialized to the Ising theory.

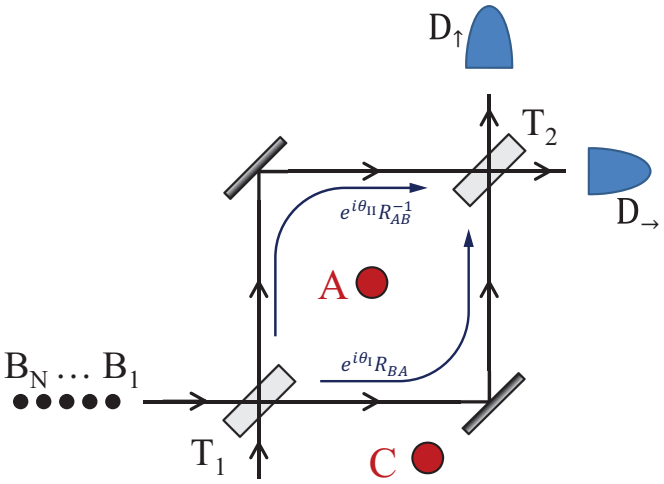

Fig. 2.1. An idealized Mach-Zehnder interferometer for an anyonic system, where T_j are beam splitters. The target anyons (collectively denoted A) in the central region share entanglement only with the anyon(s) C outside this region. A beam of probe anyons $B_1, \ldots, B_N$ is sent through the interferometer and detected at one of the two possible outputs by D_s.

2 What an Anyonic Interferometer Does in Two Different Languages

We recall the bare bones of anyonic interferometry in a general anyonic context (as developed in [1,2]; see [45] for notational clarification and calculational details).

The target anyon A may be a composite of several quasiparticles (anyons), so it is not necessarily in an eigenstate of charge. In the simplest case, which we treat, the probe quasiparticles B are assumed to be uncorrelated, identical, and simple (not composites). In fact, to make the source standard and uncorrelated, the probes will be independently drawn from the vacuum together with an antiparticle (topological charge conjugate anyon), which is then discarded and mathematically "traced out." We will simplify the discussion in this paper by also assuming the probe has definite topological charge values $B = b$, but the generalization is straightforward. Coming from the left, probe anyon B_i encounters first beam splitter T_1, and then T_2. The corresponding transition matrices are:

$$T_j = \begin{bmatrix} t_j & r_j^* \\ r_j & -t_j^* \end{bmatrix}. \tag{2.1}$$

The unitary operator representing a probe anyon passing through the interferometer is given by

$$U = T_2 \Sigma T_1 \tag{2.2}$$

$$\Sigma = \begin{bmatrix} 0 & e^{i\theta_{\mathrm{II}}} R_{AB}^{-1} \\ e^{i\theta_{\mathrm{I}}} R_{BA} & 0 \end{bmatrix}. \tag{2.3}$$

This can be written diagrammatically as

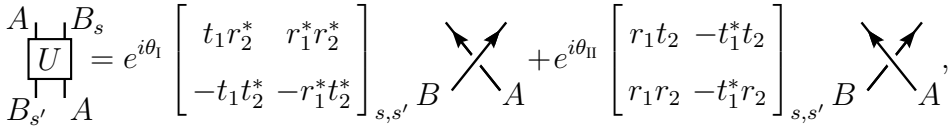

, (2.4)

where we introduce the notation of writing the directional index s of the probe quasiparticle as a subscript on its anyonic (topological) charge label, e.g. B_s. The anyonic state complementary to the region being probed will be denoted by C (and later by two disjoint sectors C_1 and C_2).

The passage of a single probe B transforms the density matrix ρ^{AC} for both system and environment by

$$\rho^{AC} \mapsto \rho^{AC}(s) = \frac{1}{\Pr(s)} \widetilde{\mathrm{Tr}}_B \left[\Pi_s V U \left(\rho^B \otimes \rho^{AC} \right) U^\dagger V^\dagger \Pi_s \right], \tag{2.5}$$

where $\widetilde{\mathrm{Tr}}$ is the "quantum trace," V represents braiding, and

$$\Pr(s) = \widetilde{\mathrm{Tr}}[\Pi_s V U \rho U^\dagger V^\dagger] \tag{2.6}$$

is the probability of measurement outcome s. The effect of this superoperator can be computed by considering the action on the ρ^{AC} density matrix's basis elements, which is expressed diagrammatically by

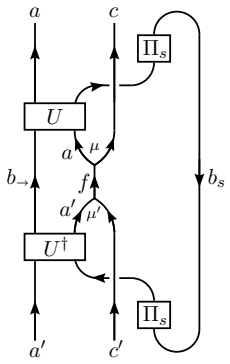

(2.7)

For the outcome $s = \rightarrow$, this may be expanded as

$$\sum_{(e,\alpha,\beta)} \left[\left(F^{ac}_{a'c'} \right)^{-1} \right]_{(f,\mu,\mu')(e,\alpha,\beta)}$$

$$\times \Bigg\{ |t_1|^2 |r_2|^2$$ 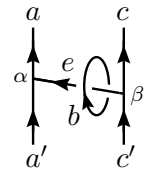

$$+ t_1 r_1^* r_2^* t_2^* e^{i(\theta_{\rm I}-\theta_{\rm II})}$$ 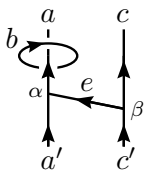

$$+ t_1^* r_1 t_2 r_2 e^{-i(\theta_{\rm I}-\theta_{\rm II})}$$ 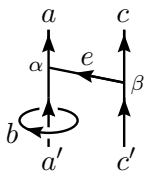

$$+ |r_1|^2 |t_2|^2$$ 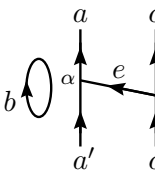

$$\Bigg\}$$

$$= d_b \sum_{\substack{(e,\alpha,\beta) \\ (f',\nu,\nu')}} \left[\left(F^{ac}_{a'c'} \right)^{-1} \right]_{(f,\mu,\mu')(e,\alpha,\beta)} p^{\vec{}}_{aa'e,b} \left[F^{ac}_{a'c'} \right]_{(e,\alpha,\beta)(f',\nu,\nu')}$$ 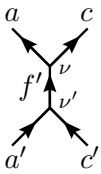

(2.8)

where we have defined

$$\begin{aligned} p^{\vec{}}_{aa'e,b} = & \left|t_1\right|^2 \left|r_2\right|^2 M_{eb} + t_1 r_1^* r_2^* t_2^* e^{i(\theta_{\rm I}-\theta_{\rm II})} M_{ab} \\ & + t_1^* r_1 t_2 r_2 e^{-i(\theta_{\rm I}-\theta_{\rm II})} M^*_{a'b} + \left|r_1\right|^2 \left|t_2\right|^2 , \end{aligned} \tag{2.9}$$

where M is the monodromy matrix $M_{ab} = \frac{S_{ab} S_{00}}{S_{0a} S_{0b}}$ (with S the modular S-matrix), and $\theta_{\rm I}, \theta_{\rm II}$ are the non-universal phases associated with traversing the interferometer via the two different paths around the interferometry region. A similar calculation for $s = \uparrow$ gives

$$\begin{aligned} p^{\uparrow}_{aa'e,b} = & \left|t_1\right|^2 \left|t_2\right|^2 M_{eb} - t_1 r_1^* r_2^* t_2^* e^{i(\theta_{\rm I}-\theta_{\rm II})} M_{ab} \\ & - t_1^* r_1 t_2 r_2 e^{-i(\theta_{\rm I}-\theta_{\rm II})} M^*_{a'b} + \left|r_1\right|^2 \left|r_2\right|^2 . \end{aligned} \tag{2.10}$$

Thus, we have the single probe measurement probabilities

$$\Pr(s) = \sum_{a,c,f,\mu} \rho^{AC}_{(a,c;f,\mu),(a,c;f,\mu)} p^{s}_{aa0,B}, \tag{2.11}$$

and post-measurement state (for outcome s)

$$\begin{aligned} \rho^{AC}(s) = & \sum_{\substack{a,a',c,c',f,\mu,\mu' \\ (e,\alpha,\beta),(f',\nu,\nu')}} \frac{\rho^{AC}_{(a,c;f,\mu),(a',c';f,\mu')}}{\left(d_f d_{f'}\right)^{1/2}} \left[\left(F^{a,c}_{a',c'} \right)^{-1} \right]_{(f,\mu,\mu')(e,\alpha,\beta)} \\ & \times \frac{p^{s}_{aa'e,B}}{\Pr(s)} \left[F^{a,c}_{a',c'} \right]_{(e,\alpha,\beta)(f',\nu,\nu')} \left|a,c;f',\nu\right\rangle \left\langle a',c';f',\nu'\right| . \end{aligned} \tag{2.12}$$

The next step (which we sketch very lightly here) is to compute probabilities and the effect for a stream of N identical probe anyons B, on ρ^{AC}. The results are:

$$\Pr\left(s_1,\ldots,s_N\right)=\sum_{a,c,f,\mu}\rho^{AC}_{(a,c;f,\mu),(a,c;f,\mu)}p^{s_1}_{aa0,B}\cdots p^{s_N}_{aa0,B}, \tag{2.13}$$

$$\begin{aligned}\rho^{AC}\left(s_1,\ldots,s_N\right)=&\sum_{\substack{a,a',c,c',f,\mu,\mu'\\(e,\alpha,\beta),(f',\nu,\nu')}}\frac{\rho^{AC}_{(a,c;f,\mu),(a',c';f,\mu')}}{\left(d_f d_{f'}\right)^{1/2}}\left[\left(F^{a,c}_{a',c'}\right)^{-1}\right]_{(f,\mu,\mu')(e,\alpha,\beta)}\\&\times\frac{p^{s_1}_{aa'e,B}\cdots p^{s_N}_{aa'e,B}}{\Pr\left(s_1,\ldots,s_N\right)}\left[F^{a,c}_{a',c'}\right]_{(e,\alpha,\beta)(f',\nu,\nu')}\left|a,c;f',\nu\right\rangle\left\langle a',c';f',\nu'\right|.\end{aligned} \tag{2.14}$$

It is clear that the specific order of the measurement outcomes is not important, but only the total number of outcomes of each type matters, and that keeping track of only the total numbers leads to a binomial distribution.

For generic choices of interferometric parameters: $t_j, r_j, \theta_{\mathrm{I}}$, and θ_{II}, these binomial distributions will concentrate exponentially fast at distinct transmission probabilities associated with the equivalence classes of charge types a where $a\equiv a'$ if and only if $M_{a,b}=M_{a',b}$. In the simplest cases, there is a natural choice for the probe B where every a is distinguished (e.g. for Ising and Fibonacci anyons one selects $b=\sigma$ and $b=\tau$, respectively), and hence the "equivalence classes" are singletons. In general, the probability of observing n (out of N) probes in the $\rightarrow$ detector is:

$$\Pr{}^{\kappa}_{N}\left(n\right)=\sum_{\kappa}\Pr{}_{A}\left(\kappa\right)\frac{N!}{n!(N-n)!}p^{n}_{\kappa}(1-p_{\kappa})^{N-n}, \tag{2.15}$$

$$\Pr{}_{A}\left(\kappa\right)=\sum_{a\in\mathcal{C}_\kappa,c,f,\mu}\rho^{AC}_{(a,c;f,\mu),(a,c;f,\mu)}, \tag{2.16}$$

where κ indexes the equivalence classes $\mathcal{C}_\kappa$ w.r.t. probe b. The fraction $r=n/N$ of probes measured in the $s=\!\!\rightarrow$ detector goes to $r=p_\kappa$ with probability $\Pr_A(\kappa)$, and the target anyon density matrix will generically collapse onto the corresponding "fixed states."

The asymptotic operation $N\rightarrow\infty$ of a generically tuned anyonic interferometer converges to a fixed state of charge sector κ with probability $\Pr_A(\kappa)$ and: 1) projects the anyonic state onto the subspace where the A anyons have collective anyonic charge in $\mathcal{C}_\kappa$, and 2) decoheres all anyonic entanglement between subsystem A and C that the probes can detect. The sector κ may be a single charge or a collection of charges with identical monodromy elements with the probes, i.e. $M_{a,B}=M_{a',B}$ for $a,a'\in\mathcal{C}_\kappa$. The anyonic entanglement between A and C is described in the form of anyonic charge lines connecting these subsystems, i.e. the charge lines labeled by charge e in the preceding analysis, where the contribution of a diagram to the density matrix will be removed if $M_{e,B}\neq 1$. Convergence to such a fixed state is

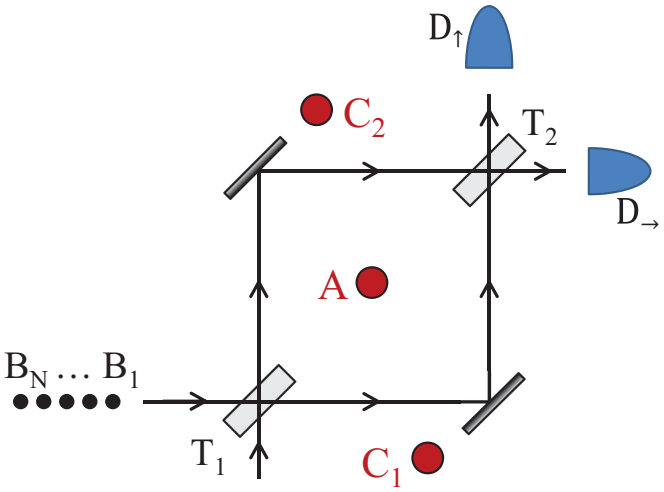

Fig. 2.2. An idealized Mach-Zehnder interferometer where the anyons C entangled with the target anyons A are separated into two regions C_1 and C_2.

based on Gaussian statistics, therefore exponentially precise as a function of the number N of probe particles.

In the simplest case, $M_{a,b} = M_{a',b} \Rightarrow a = a'$ and the indistinguishable equivalence classes $C_{\kappa_a} = \{a\}$ are singletons, i.e. all topological charges are distinguished. The corresponding fixed state density matrix is:

$$\rho_{\kappa_a}^{AC} = \sum_c \frac{\Pr_A(c|a)}{d_a d_c} \mathbb{I}_{ac} = \sum_{c,f',\nu} \frac{\Pr_A(c|a)}{d_a d_c} |a,c;f',\nu\rangle\langle a,c;f',\nu|, \qquad (2.17)$$

where

$$\Pr_A(c|a) = \frac{\sum_{f,\mu} \rho^A_{(a,c;f,\mu)(a,c;f,\mu)}}{\sum_{c,f,\mu} \rho^A_{(a,c;f,\mu)(a,c;f,\mu)}}. \qquad (2.18)$$

(The formulae for the general case can be found in [1,2].) From this point on, we focus only on these cases where the probe distinguishes all topological charges.

This is a convenient place to note a modest generalization, where the complementary charge C is divided into two regions separated by the interferometer, which we similarly denote as C_1 and C_2, respectively. In some experimental setups — e.g. a Fabrey-Pérot interferometer on a quantum Hall bar — each arm of the interferometer individually will separate the region with charge A from a complementary region with respective charges C_1 and C_2, which could both be nontrivial. This situation is depicted for the idealized Mach-Zehnder interferometer in Fig. 2.2. In this circumstance, all charge lines from A to C_1 and from A to C_2 are (separately) decohered if they can be detected by the probes B.

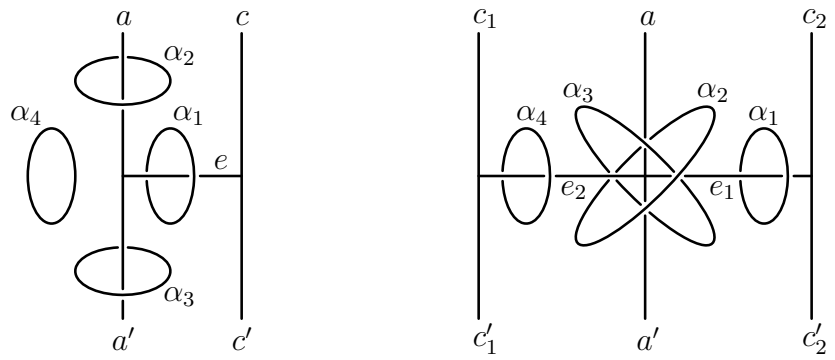

Fig. 2.3. (a) For a single region of complementary anyons C, we show the four positions for the probe loops corresponding to the four terms of Eq. (2.8). (b) For two regions of complementary charge C_1 and C_2, the four positions of probe loops are shown on the more complicated the target system (with complementary anyons) density matrix components. (The 4-valent vertex is understood to be resolved into appropriate trivalent vertices.) α_j denotes the weight with which the corresponding probe loop configuration enters the measurement superoperator.

In Fig. 2.3, we compare the diagrammatic terms that arise for a single C region formulation to when there are two regions C_1 and C_2. For probe b and measurement outcome $s =\!\rightarrow$, the four probe loop configurations enter the measurement superoperator with weights

$$\alpha_1^{\rightarrow} = |t_1|^2|r_2|^2, \tag{2.19}$$
$$\alpha_2^{\rightarrow} = t_1 r_1^* r_2^* t_2^* e^{i(\theta_I - \theta_{II})}, \tag{2.20}$$
$$\alpha_3^{\rightarrow} = t_1^* r_1 t_2 r_2 e^{-i(\theta_I - \theta_{II})}, \tag{2.21}$$
$$\alpha_4^{\rightarrow} = |r_1|^2|t_2|^2, \tag{2.22}$$

as in Eq. (2.8). For $s =\!\uparrow$, these are

$$\alpha_1^{\uparrow} = |t_1|^2|t_2|^2, \tag{2.23}$$
$$\alpha_2^{\uparrow} = -t_1 r_1^* r_2^* t_2^* e^{i(\theta_I - \theta_{II})}, \tag{2.24}$$
$$\alpha_3^{\uparrow} = -t_1^* r_1 t_2 r_2 e^{-i(\theta_I - \theta_{II})}, \tag{2.25}$$
$$\alpha_4^{\uparrow} = |r_1|^2|r_2|^2. \tag{2.26}$$

Given N uncorrelated identical probe anyons, there are 4^N configurations of probe loops, each probe choosing from the four positions, with the single probe weights (depending on a given probe's measurement outcome) being multiplied together for the overall superoperator. For the two probe loop positions which cross in Fig. 2.3(b), repeated copies will nest according to the pattern of later probe loops having larger radius. We will see shortly that the detail of the nesting patterns are irrelevant in the large N limit.

According to the calculation just summarized, the net effect of running the interferometer on the target system with density matrix ρ^{AC}, up to corrections that decay exponentially in N, is that the superposition of these 4^N configurations results in a measurement of the collective charge of anyons A onto charge value a, with probability

$$\Pr_{AC}(a) = \widetilde{\mathrm{Tr}}\left[\rho^{AC}\Pi_a^A\right], \tag{2.27}$$

and post-measurement density matrix

$$\rho_a^{AC} = \frac{1}{\Pr_{AC}(a)}$$

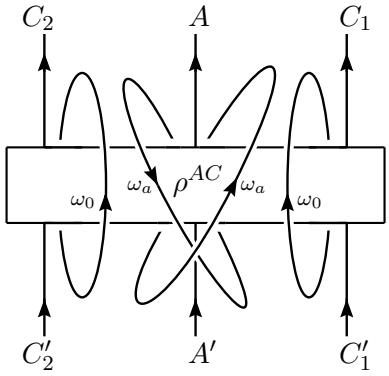

. (2.28)

(All topological charge lines drawn here have zero framing, i.e. there are no twists in the frame.) The ω_a-loops

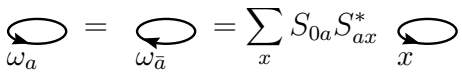

$$= \sum_x S_{0a}S_{ax}^* \tag{2.29}$$

have the effect of projecting all charge lines passing through the loop onto collective charge a. Thus, the ω_0-loops effectively cut charge lines. This allows the ω_a-loops to be moved to encircle only the A and A' lines, i.e. one can perform a handle slide of the loop around the ω_0-loops (see Section 3.1). Thus, the ω_a-loops effect projection of anyons A into collective charge sector a. When there is only one region of complementary anyons C, e.g. if there are no C_2 anyons, then the action of the ω_0-loop between A and C_2 is trivial. Notice that the ω-loops here occur in precisely the same positions as the four possible probe loop configurations.

Having depicted the effect of interferometry in terms of ω-loops, we make a geometric observation for later use: the effects of interferometry are localized to a certain quasi-1D region of space-time surrounding the ω-loops called a "handle body." These are indicated in Fig. 2.4 as the regions H and H' for the single region C and two region C_1 and C_2 configuration of complementary anyons. The handlebodies H and H' model the complementary regions surrounding the ρ^{AC} density matrix operator. This enables us to make calculations for twisted interferometry simply by computing operators within transformed coordinates.

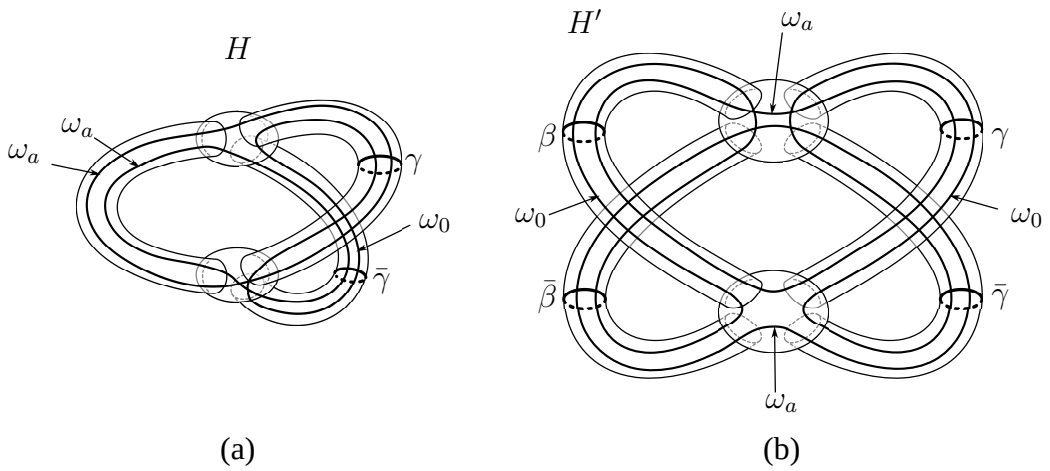

(a) (b)

Fig. 2.4. (a) Genus 2 handle body H and (b) genus 3 handle body H', within which the effect of interferometry is localized in Eq. (2.28). Some curves in ∂H and $\partial H'$ are labeled for later reference.

3 Topological Explanations

The goal of this section is to explain the topological nature of interferometry. In Section 3.1, we first review some pure topology background on 3-manifold surgery and the handle slide property. In Section 3.2, we apply this machinery to interferometry, with the basic idea being that in the limit of large N, the exact partition function, given by 4^N terms with probe anyon Wilson loops, can effectively be described by a small number of Dehn surgeries. Although this abstract topological approach may at first seem like overkill, it proves its utility when we try to generalize to the case of twisted interferometry, which is introduced in Section 3.3. Indeed, as shown in Section 3.4, twisting has a natural description in the effective topological language: to compute the partition function in the twisted case, all we have to do is modify the gluing of a certain handle body by some twists. Section 3.5, although not necessary in the logical flow of the paper, develops a stand-alone, purely topological perspective on interferometry. Finally, in Section 3.6, we apply all this machinery to the case of the Ising UMTC, and describe the simplifications that arise.

3.1 Surgery and the Handle Slide Property

"Handles" are a combinatorial tool for assembling smooth d-manifolds with boundary out of little pieces, which are individually copies of d-balls. Our main focus is $d = 4$, since we will manipulate within a $(2+1)$D TQFT using a representation where the 3D space-time is the boundary of a 4D bulk. Note, however, that the handle bodies drawn in Fig. 2.4 are 3D, being subsets of the space-time itself.

Let B^d denote the unit ball in $\mathbb{R}^d$. There are $d+1$ types of d-dimensional han-

dles, called k-handles (or handles of index k), where $0 \leq k \leq d$. A k-handle is a pair $(B^k \times B^{d-k}, \partial B^k \times B^{d-k})$. Note that the total space $B^k \times B^{d-k}$ is always diffeomorphic to a d-ball B^d, so what is significant is the portion of the boundary specified in the second slot. This portion is called the "attaching region" and consists of larger portions of ∂B^d as the index k increases. For example, the five k-handles for dimension $d = 4$ are given by:

k	attaching region
0	$\varnothing$ = nothing
1	$\{-1, 1\} \times B^3$ = two balls
2	$S^1 \times B^2$ = solid torus
3	$S^2 \times I$ = spherical shell
4	S^3 = entire 3-sphere

(3.1)

We see from this table:

0-handles are attached to nothing; they are the beginning of the construction of a 4-manifold M^4, corresponding to local minima of the Morse function, $x_1^2 + x_2^2 + x_3^2 + x_4^2 = 0$.

1-handles attach to 0-handles, and correspond to an index = 1 saddle, $-x_1^2 + x_2^2 + x_3^2 + x_4^2$.

2-handles attach to the union of 0- and 1-handles and correspond to an index = 2 saddle $-x_1^2 - x_2^2 + x_3^2 + x_4^2$.

3-handles attach to the previous union of 0-, 1-, and 2-handles and correspond to an index = 3 saddles, $-x_1^2 - x_2^2 - x_3^2 + x_4^2$.

4-handles correspond to a local maxima, $-x_1^2 - x_2^2 - x_3^2 - x_4^2$.

An interesting aspect of handle bodies is that there are moves which slide one k-handle h_1, over a second k-handle h_2, which change the attaching maps, but do not change the diffeomorphism type of the manifold being described. The geometric operation of sliding one 2-handle over another has an algebraic analog in the diagrammatic formalism of TQFTs and UMTCs. First, we explain the geometric move and then the analog.

Passing a 2-handle h_1 over another h_2 means transforming the two solid tori attaching regions, drawn as framed loops in a 3-manifold, as shown in Fig. 3.1(a) and (b). The framing describes how $\partial B^2 \times B^2$ is identified or "glued" to a neighborhood of the loop. An idea of how the 4D-handles are sliding is given by the sketch in Fig. 3.1(c) and (d), in which the dimensions have been cut in half.

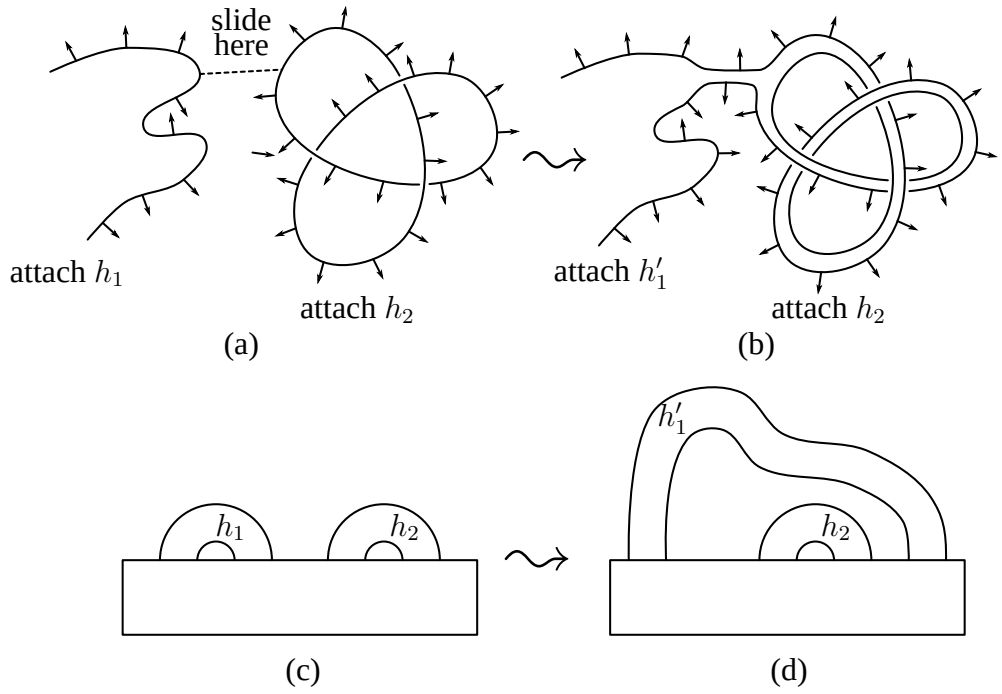

Fig. 3.1. Sliding handles.

As far as the effect on the boundary 3-manifold is concerned, the attachment of a 2-handle realizes a surgery (sometimes called Dehn surgery), meaning that the solid torus to which the attaching region is glued is removed and then another replacement solid torus, in this case $B^2 \times \partial B^2$, is glued back in. The meridional loop, $\partial B^2 \times *$ of the new solid torus, matches with whichever longitude on the original solid torus is dictated by the framing vector. From this point of view, the rules (Table 3.1) for sliding handles amounts to a way of recognizing that surgery on two different framed links yield the same 3-manifold, after surgery. The subject which decides when two framed links yield (upon surgery) the same 3-manifold is often called "Kirby calculus."

The following diagrammatic calculation

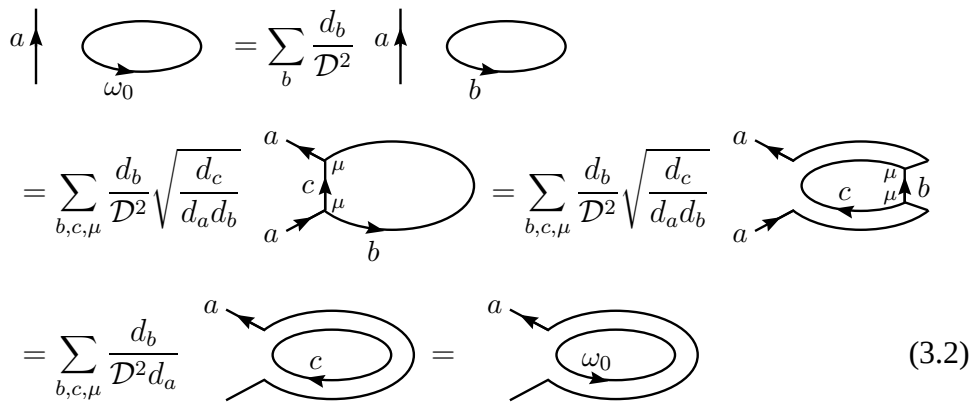

(3.2)

establishes the handle slide property for ω_0-loops. This shows that, within the UMTC formalism, if a framed loop γ_2 is an ω_0-loop, then the partition function Z is unaffected by sliding an arbitrarily labeled loop γ_1 over γ_2. For simplicity, in Eq. (3.2), we have shown only an arc segment of γ_1 (labeled with charge a) and γ_2 as an ellipse, but one may think of γ_2 as a knot, as in Fig. 3.1. Thus, a loop labeled by ω_0 has the same handle slide property as a 2-handle h_2. This justifies interpreting ω_0-labeled framed loops in all diagrams of states or density matrices as being "surgered." That is, the diagram effectively exists in a topologically exotic space-time 3-manifold created by surgery on the ω_0-loops, and therefore consists only of the loops not labeled by ω_0.

There is an immediate generalization from ω_0-loops to ω_a-loops. After doing the surgery indicated by ω_0, the loop labeled by a slides into a copy of the core $0 \times \partial B^2 \subset B^2 \times \partial B^2$ of the replacement solid torus (with product normal framing). Thus, any loop labeled by ω_a may also be interpreted as surgered out in the effective diagram, but with the difference that there will now be a Wilson loop with charge a (and product framing) running along the core of the replacement solid torus. This is represented diagrammatically by

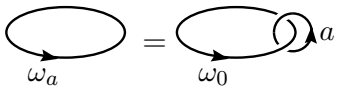

(3.3)

Similarly, one can formally sum over the charge values a of ω_a-loops in such diagrams.

In general, curves labeled by ω_a do not have a particularly convenient handle slide property. However, there is a nice identity for sliding an ω_a-loop over an ω_b-loop when b is an Abelian anyon:

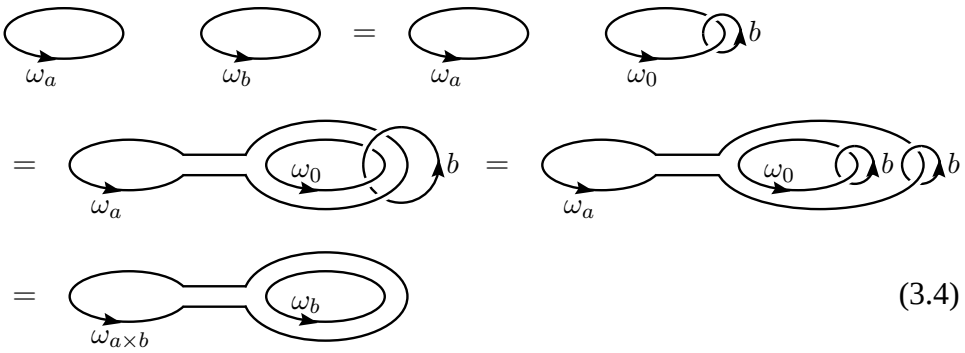

(3.4)

This identity will play a key role in simplifying the analysis of both twisted and untwisted interferometers in Ising-type systems, as it allows us to slide ω_a-loops over ω_b-loops when $b = \psi$ is the (Abelian) fermion charge of the Ising theory.

Using the handle slide property of ω_0-loops, the post-measurement density matrix of Eq. (2.28) can be rewritten (as previously mentioned) as

$$\rho_a^{AC} = \frac{1}{\Pr_{AC}(a)}$$

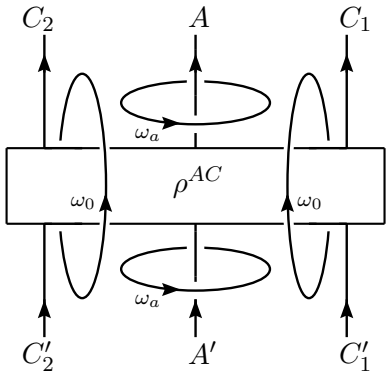

. (3.5)

Note that the use of two ω_a-loops here is redundant, since one can move one of them to the other one's position using handle slide and ω-loops are idempotent (i.e. they are projectors).

3.2 The Effective Surgical Description of Interferometry

The density matrix formalism replaces a state vector $|\psi\rangle$ with a state operator ρ, equal to $\rho = |\psi\rangle\langle\psi|$ for a pure state. Similarly in the density matrix formalism, a space-time evolution in $\mathrm{Hom}(W, V)$ carrying an initial ψ_0 to ψ_1 becomes an operator in $V^* \otimes V$ by forming $\mathrm{Hom}(W, V) \otimes \mathrm{Hom}^*(W, V)$ and tracing out W. Topologically, the density matrix components are (superpositions of) diagrams in a space-time glued to a copy of itself reflected across a time $t = 0$ plane. The diagrams in Eqs. (2.28) and (3.5) should be interpreted in this way.

In topological language, the conclusion of Refs. [1,2,45], as recapitulated in Sec-

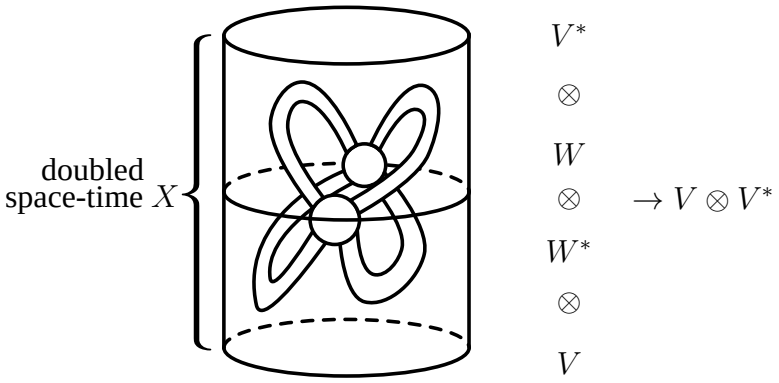

Fig. 3.2. Density matrix as a diagram in space-time glued to a reflected copy of itself.

tion 2 is that (up to exponentially suppressed corrections) the effective diagram for the partition function is the probabilistic combination of Dehn surgeries and Wilson loops indicated in Fig. 2.4. Note that, while the exact partition function is given by 4^N terms with probe anyon Wilson loops, the effective diagram has no probe anyons in it. It only has a small number of Dehn surgeries, some with Wilson loops at the core. Surgeries on ω_0-loops are "ordinary" and for the ω_a-loop surgeries, one input is a probabilistically determined charge a along the core circle (Wilson loop) of the replacement solid torus. This may also involve a sum of simple charges $\omega_{\mathcal{A}} = \sum_{a\in\mathcal{A}} \omega_a$, if one wishes to treat the case where the probe anyons do not distinguish all topological charge types, i.e. $M_{a,b} = M_{a',b}$ for all $a, a' \in \mathcal{A}$. In this case, the Wilson loop has a superposition of charges $a \in \mathcal{A}$, i.e. is treated as a formal linear combination of diagrams.

3.3 Twisted Interferometers

Now that we have established the topological language, the modification necessary to compute the effect on the partition function Z of twisting the arms amounts to cutting the handle-body H out of the doubled space-time and gluing back in with certain twists.

3.4 Computing the Consequence of Twisting

The operation of an idealized anyonic interferometer is described by a few (generalized) surgeries within the handle body H or H' inside the doubled space-time manifold X, as shown in Fig. 2.4. In this surgery formulation, introducing probe anyon twisting into the arms of the interferometer is accounted for by removing the handle body H or H' from the doubled space-time and then re-gluing it back into $X \setminus H$ or $X \setminus H'$, respectively, with additional twists as shown in Fig. 3.4.

Let l and r represent the number of full twists imposed on the left and right arms,

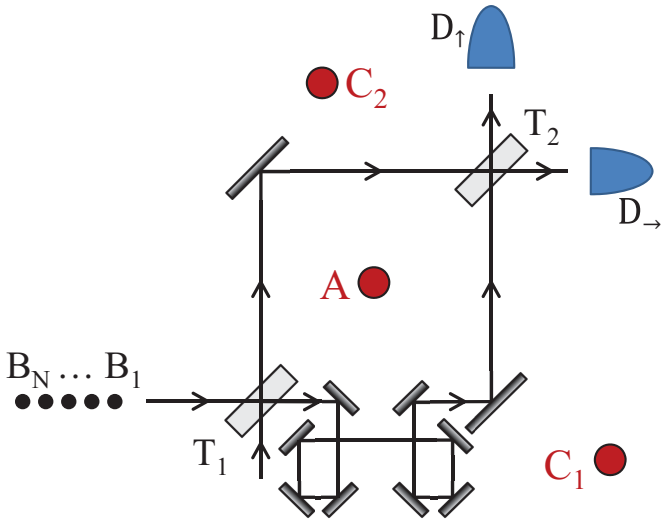

Fig. 3.3. An idealized Mach-Zehnder anyonic interferometer with a doubly twisted path in its right arm.

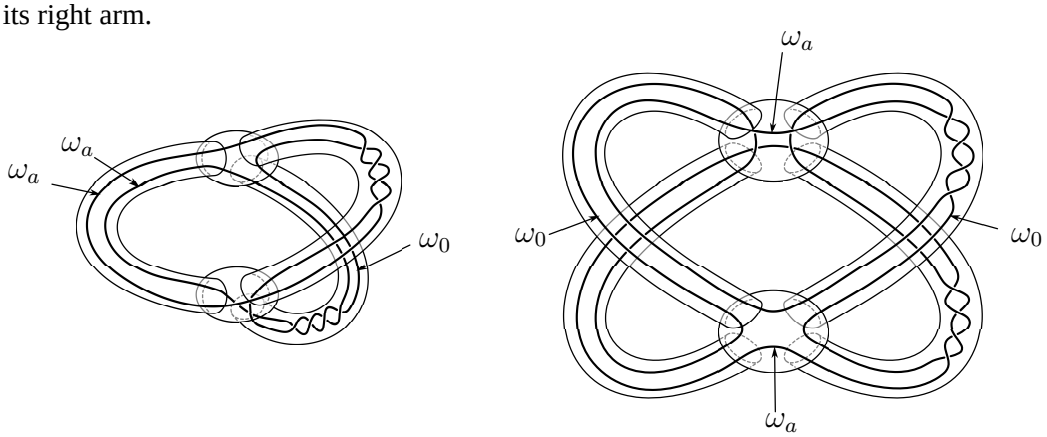

(a) (b)

Fig. 3.4. (a) $H \subset X$ and (b) $H' \subset X$ re-glued back into the doubled space-time X after introducing twists into the handles. Here we show the twisting, $+2$ Dehn twists applied to γ and -2 Dehn twists applied to $\bar{\gamma}$, corresponding to a double twist implemented in the right arm of the interferometer.

respectively. The appropriate re-gluing of H or H' is induced by a number of Dehn twists applied to the loops $\beta, \bar{\beta}, \gamma, \bar{\gamma}$ in Fig. 2.4 according to the rules

loop	# of Dehn twists
γ	r
$\bar{\gamma}$	$-r$
β	l
$\bar{\beta}$	$-l$

(3.6)

The effect of opposite (mirror image) twisting leaves the framing of the ω_0-labeled curves unchanged. In the re-glued H or H', the ω_a-loops and ω_0-loops are repositioned as shown in Fig. 3.4 for $r = 2$ and $l = 0$, i.e. an interferometer with a double twist in its right arm.

Thus, the conclusion of our topological/diagrammatic analysis is:

Using the computational rules inherent in the definition of a (2+1)D TQFT (i.e. UMTC), the effective result of (l, r)-twisted anyonic interferometers (ignoring exponentially suppressed corrections, multiple passes, and probe-probe interactions) by inserting the Wilson loops, as shown in Fig. 3.4 for $(l, r) = (0, 2)$, as in Fig. 2.4 with Dehn twists applied to the loops γ, $\bar{\gamma}$, β, and $\bar{\beta}$ according to the rules in Eq. (3.6) and evaluating the density matrix Z. Diagrammatically, this can be represented by

$$\tilde{\rho}_a^{AC} = \frac{1}{\tilde{\Pr}_{AC}(a)}$$

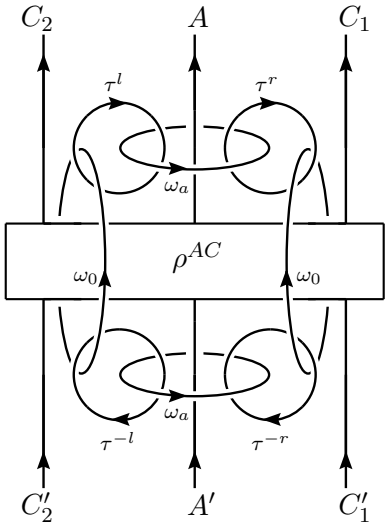

(3.7)

where a τ^m-loop, given by

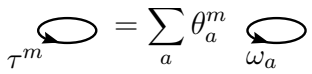

(3.8)

is equivalent to the application of m twists to all the topological charge lines passing through the loop, and $\tilde{\Pr}_{AC}(a)$ is the probability of twisted charge measurement outcome a by the twisted interferometer. The τ^m-loops here correspond to the γ, $\bar{\gamma}$, β, and $\bar{\beta}$ curves in the handle bodies.

3.5 Topological Understanding

We have used local diagrammatic calculations [1,2,45] as input to topological machinery. The output has been the surgical operation described in Section 3.4. It is also possible, retrospectively, to give an illuminating, if not rigorous, topological

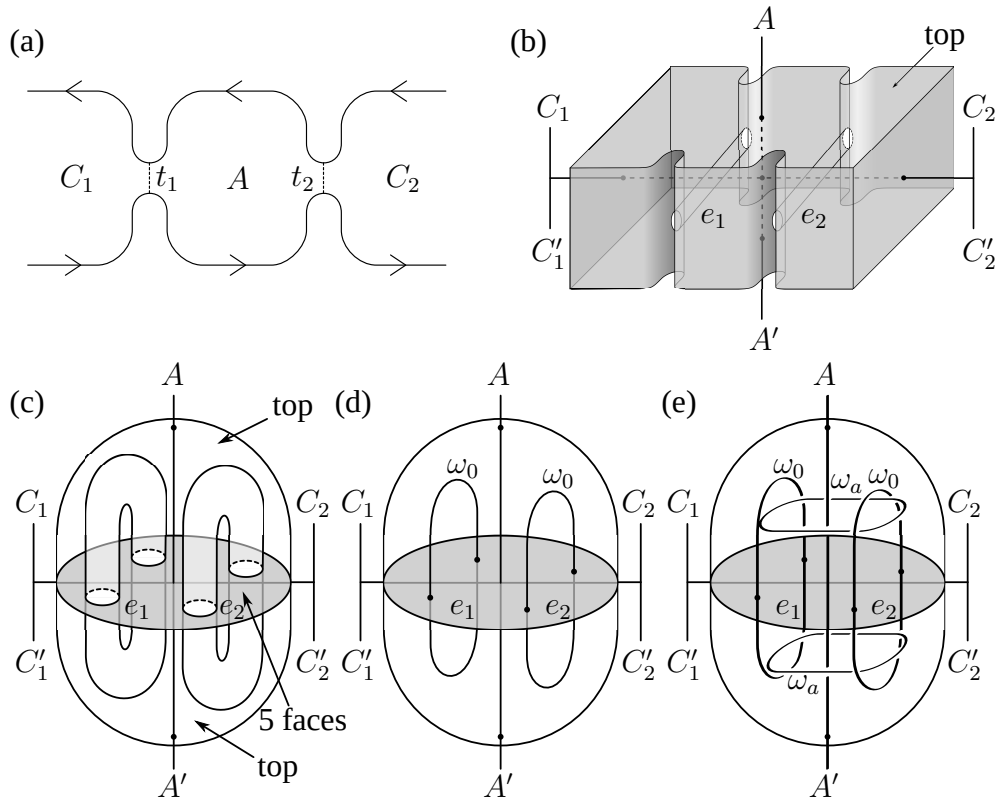

Fig. 3.5. (a) Spatial configuration of a fractional quantum Hall double-point contact interferometer. (b) Space-time description, including tunneling events, represented by evacuations of topological fluid. (c) Doubling the space-time along the five shaded faces (bottom and 4 sides) and gluing each tube to its mirror image. (d) Collapsing the tubes in (c) to Wilson lines, labeled by ω_0. (e) Doubling space-time, gluing tubes to their cross components (i.e. the interference terms), and collapsing the tubes gives rise to the ω_a-loops.

explanation of the rules derived in [45] through the diagrammatic method. To give this explanation, it is convenient to think of a fractional quantum Hall double point-contact (Fabrey-Pérot) interferometry in the low tunneling limit (where its effect is essentially the same as the idealized Mach-Zehnder). In Fig. 3.5, we draw the space-time history of the topological fluid. We take the point of view that the fluid has been "evacuated" along tubes representing the collective tunneling path of the probes and that, because a large and indeterminate number of probes have passed, we know nothing about the effective topological charge on the meridians of these tubes. (The meridional topological charge could be any fusion product of multiple probe anyons. The probe quasiparticles in most cases will have small effective mass and correspond to edge theory tunneling operators with lowest scaling exponents (conformal dimensions), from which all other quasiparticles can be generated as composites.) To produce the manifold (with framed Wilson lines) X corresponding to the partition function Z, we should double the space-time history along its boundary and past, and then further trace out unknown degrees of freedom on the meridians of the tubes by gluing each tube boundary to its mirror image. This last step folds each longitude loop γ over itself to become an arc α. Topologically, this

is precisely what a zero-framed surgery accomplishes. The latter provides a disk Δ for each longitude loop γ to bound, but after providing Δ, it is topologically equivalent to then projecting Δ to one of its coordinates, resulting in the arc α. The surgeries are encoded by the ω_0-loops in Fig. 3.5(d) and (e). Gluing a tube to its mirror image means that each longitudinal circle γ = (transversal arc) $\cup$ (mirror image transversal arc) gets collapsed to a single arc α. Topologically, this is equivalent to providing a disk of space-time topological fluid to span across each longitudinal circle: $\partial B^2 \times *, * \in \partial B^2_{\text{second factor}}$.

This explains, via the surgery/handle attachment picture, the passage from (c) to (d) in Fig. 3.5. We can represent the glued tubes as two new Wilson loops labeled by ω_0, as explained in Section 3.1. The final frame Fig. 3.5(e) includes the ω_a-loops reflecting what the interferometer was "intended" to do, i.e. project A into topological charge sector a by measuring the interference term between the two tunneling paths. From this point of view, the ω_0-loops are an "unintended" consequence of running the interferometer: tunneling the stream of probes anyons B "inadvertently" decohered system A from it complementary anyons C_1 and C_2.

3.6 The Ising Theory

The twisted interferometry analysis represents a completely general tool for investigating the effects in general (2+1)D anyonic systems. However, we are primarily interested in the application for the Ising-type TQFTs, as these are the most physically practical non-Abelian anyonic systems to physically realize and are also the only examples we know (so far) that twisted interferometry provides an enhancement of computational utility. Ising TQFTs have topological charges I (vacuum), σ (non-Abelian anyon), and ψ (fermion), where the σ anyon should have a (statistical) twist factor $\theta_\sigma = e^{2\pi i x/16}$ for x odd. This is the crucial T-matrix entry. In our calculation, we take $x = 1$, but the other choices yield similarly useful results. The remainder of this paper is focused on this case.

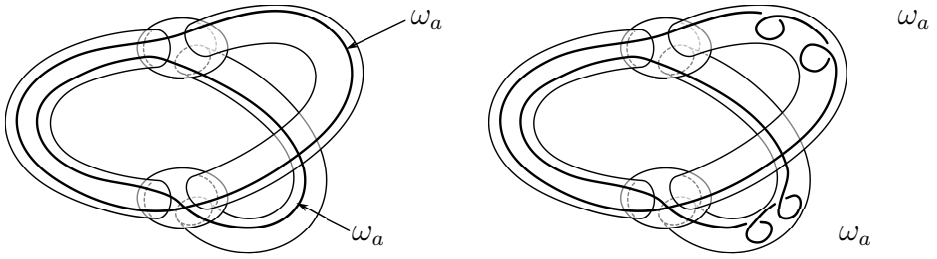

(a) (b)

Fig. 3.6. Genus 2 handle bodies for (a) untwisted and (b) twisted interferometry using Ising anyons when $a = I$ or ψ.

For convenience, we recall the fusion and braiding properties of the Ising MTC

$\mathcal{C} = \{I, \sigma, \psi\}, \quad I \times a = a, \quad \sigma \times \sigma = I + \psi, \quad \sigma \times \psi = \sigma, \quad \psi \times \psi = I$	
$[F_\sigma^{\sigma\sigma\sigma}]_{ef} = [F_{\sigma\sigma}^{\sigma\sigma}]_{ef} = \begin{bmatrix} \frac{1}{\sqrt{2}} & \frac{1}{\sqrt{2}} \\ \frac{1}{\sqrt{2}} & \frac{-1}{\sqrt{2}} \end{bmatrix}_{ef}$ $\left[F_\psi^{\sigma\psi\sigma}\right]_{\sigma\sigma} = \left[F_\sigma^{\psi\sigma\psi}\right]_{\sigma\sigma} = \left[F_{\psi\sigma}^{\sigma\psi}\right]_{\sigma\sigma} = \left[F_{\sigma\psi}^{\psi\sigma}\right]_{\sigma\sigma} = -1$	
$R_I^{\sigma\sigma} = e^{-i\frac{\pi}{8}}, \quad R_\psi^{\sigma\sigma} = e^{i\frac{3\pi}{8}}, \quad R_\sigma^{\sigma\psi} = R_\sigma^{\psi\sigma} = e^{-i\frac{\pi}{2}}, \quad R_I^{\psi\psi} = -1$	
$S = \frac{1}{2}\begin{bmatrix} 1 & \sqrt{2} & 1 \\ \sqrt{2} & 0 & -\sqrt{2} \\ 1 & -\sqrt{2} & 1 \end{bmatrix}$	$M = \begin{bmatrix} 1 & 1 & 1 \\ 1 & 0 & -1 \\ 1 & -1 & 1 \end{bmatrix}$
$d_I = d_\psi = 1, \quad d_\sigma = \sqrt{2}, \quad \mathcal{D} = 2$	$\theta_I = 1, \quad \theta_\sigma = e^{i\frac{\pi}{8}}, \quad \theta_\psi = -1$

The F-symbols and R-symbols not listed here are trivial, meaning they are equal to 1 if allowed by the fusion rules.

The identity in Eq. (3.4) simplifies Figs. 2.4(a) and 3.4(a) in the cases where we have a priori information (as will be present in the qubit context) that the topological charge A (corresponding to the fusion channel of a pair of anyons from a 4 anyon topological qubit) is a linear combination of I and ψ, so that the only possible ω_a-labeled Wilson loops will have $a = I$ or ψ (here we write I for 0). This is exhibited in Fig. 3.6, where we show the corresponding simplifications of Figs. 2.4(a) and 3.4(a) for the Ising theory. In particular, the ω_0-loop in those figures is redundant. This can be seen from the following argument. Using the fact that ω_a is idempotent, the upper ω_a-loop can be replaced with two parallel ω_a-loops, without changing the partition function Z. Next take one of the newly created upper ω_a-loops and slide it over the lower ω_a-loop using Eq. (3.4). The resulting loop, which now is labeled with an ω_0, may finally be isotopied into the position of the ω_0-loop in Figs. 2.4(a) and 3.4(a). Thus, these configurations of ω-loops are equivalent, demonstrating the redundance of the ω_0-loop. An analogous argument similarly shows that only the

ω_a-loops need be considered for Ising anyons with $a = I$ or ψ in Figs. 2.4(b) and 3.4(b), when the complementary anyons are in two regions C_1 and C_2.

The conclusion is that when measuring topological qubits in Ising-like theories, it is harmless to omit the surgery (i.e. the ω_0-loop) representing decoherence from a connected environment C. In the untwisted case, interferometry only gives projective measurement of the topological charge, with no decoherence of anyonic entanglement. In other words, the interferometry measurement superoperator takes pure states to pure states. This simplifies the calculation, allowing us to work with a single, rather than a doubled copy of space-time, since no surgery loops traverse the two factors.

In the case of two twists, $(r, l) = (2, 0)$, as we will compute in Section 4, the twisted interferometer (using probes with $b = \sigma$) acts on a state $|\Psi\rangle = \alpha|I\rangle + \beta|\psi\rangle$ by sending it to $|\Psi'\rangle = (1 + e^{-2\pi i/8})\alpha|I\rangle + (1 - e^{2\pi i/8})\beta|\psi\rangle$, if the "twisted measurement outcome" is charge $a = I$ and to $|\Psi'\rangle = (1 - e^{2\pi i/8})\alpha|I\rangle + (1 + e^{-2\pi i/8})\beta|\psi\rangle$ for $a = \psi$. Similarly, on the level of density matrices, for the initial target system density matrix [1]

$$\rho^{AC} = \sum_{a,a'=I,\psi} \rho^{AC}_{(a,a;I)(a',a';I)} \, |a, a; I\rangle \langle a', a'; I| = \begin{bmatrix} \rho_{00} & \rho_{01} \\ \rho_{10} & \rho_{11} \end{bmatrix}, \tag{3.9}$$

the outcome after twisted interferometry with outcomes $a = I$ or ψ are, respectively and resulting (fixed state) density matrices

$$\tilde{\rho}_I = \frac{1}{\tilde{\Pr}_{AC}(I)} \begin{bmatrix} \cos^2\left(\frac{\pi}{8}\right)\rho_{00} & i\cos\left(\frac{\pi}{8}\right)\sin\left(\frac{\pi}{8}\right)\rho_{01} \\ -i\cos\left(\frac{\pi}{8}\right)\sin\left(\frac{\pi}{8}\right)\rho_{10} & \sin^2\left(\frac{\pi}{8}\right)\rho_{11} \end{bmatrix}, \tag{3.10}$$

$$\tilde{\rho}_\psi = \frac{1}{\tilde{\Pr}_{AC}(\psi)} \begin{bmatrix} \sin^2\left(\frac{\pi}{8}\right)\rho_{00} & -i\cos\left(\frac{\pi}{8}\right)\sin\left(\frac{\pi}{8}\right)\rho_{01} \\ i\cos\left(\frac{\pi}{8}\right)\sin\left(\frac{\pi}{8}\right)\rho_{10} & \cos^2\left(\frac{\pi}{8}\right)\rho_{11} \end{bmatrix}, \tag{3.11}$$

with corresponding probabilities

$$\tilde{\Pr}_{AC}(I) = \cos^2(\pi/8)\,\rho_{00} + \sin^2(\pi/8)\,\rho_{11}, \tag{3.12}$$

$$\tilde{\Pr}_{AC}(\psi) = \sin^2(\pi/8)\,\rho_{00} + \cos^2(\pi/8)\,\rho_{11} \tag{3.13}$$

Importantly, in the twisted case, regardless of whether the redundant ω_0-loop is included in the diagram, there is no decoherence of anyonic entanglement between the target anyons A and their complementary anyons C, and the final state may

[1] The expression in terms of the qubit density matrix ρ use the qubit basis states given by $|0\rangle = |I, I; I\rangle$ and $|1\rangle = |\psi, \psi; I\rangle$.

possess coherent superposition of topological charges and anyonic entanglement between A and C. This seemingly paradoxical fact is explained by the fact that the ω_0-loop, which normally causes decoherence between A and C for the untwisted case, is (double) twisted around the two ω_a-loops. When twisted in this manner, the ω_0-loop no longer separates the target system A from C.

4 The Double Twisted Interferometer in Ising Systems

In this section, we calculate the asymptotic effect of running a twisted interferometer with two twists in one arm, as indicated in Fig. 3.3, for a system with Ising non-Abelian anyons. We are interested in a configuration where the anyons A are composed of a pair of σ anyons, which may be part of a topological qubit (requiring at least two complementary σ anyons in C) and can have collective fusion channel values I and ψ. The probe quasiparticles are assumed to carry topological charge $b = \sigma$. With appropriate assumptions, the analysis also extends to other twisted interferometer designs, such as those described in [45]. In the first two subsections, we review general TQFT technology. The effect of the twisting is computed in the final subsection.

4.1 Gluing 3-Manifolds and Tensor Contractions

The basic structure of a TQFT is a functor that assigns Hilbert spaces $H(\Sigma)$ to a surface Σ and partition functions $Z(M)$ to 3-manifolds M. If M is closed (compact and without boundary, $\partial M = \varnothing$), then the partition function $Z(M)$ is a scalar. If M has a single boundary component Σ, then $Z(M) \in H(\Sigma)$. If ∂M is divided into two pieces, say incoming and outgoing with respect to the orientation of M, then $Z(M) \in \mathrm{Hom}(H(\Sigma_{\mathrm{in}}), H(\Sigma_{\mathrm{out}}))$. The division of ∂M into pieces may be according to components, but this is not essential. Several boundary components may be grouped into one piece and one component may be cut apart along non-intersecting simple closed curves (SCCs) into two or more pieces. When SCCs are present, the boundary pieces Σ_i themselves have boundary and the appropriate Hilbert space $H(\Sigma_i)$ is a direct sum (scaled according to quantum dimensions) of all admissible topological charge labelings of the boundary components. In any case, if ∂M is divided into k pieces, the TQFT assigns a k-tensor to M. Orientation conventions determine which indices are covariant and which are contravariant.

The "Atiyah axiom," which is the fundamental gluing relation, is:

$$Z(M \cup N) = \langle Z(M), Z(N) \rangle \tag{4.1}$$

where M and N are glued over a common piece of boundary and the symbol $\langle \cdot, \cdot \rangle$,

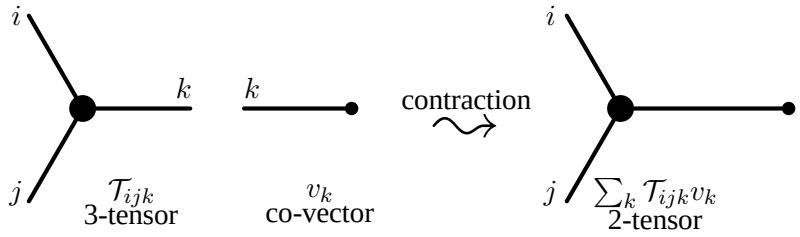

Fig. 4.1. Tensor contraction.

suggestive of the inner product, means contract the tensors along the index associated to the glued piece of boundary.

For example, if M has among its boundary components a torus T and $N = S^1 \times D^2$ is a solid torus with boundary identified to T (N may contain a charged Wilson loop at its core), then $Z(M \cup N)$ is obtained as a tensor contraction as in Fig 4.1.

As we run interferometers (twisted or untwisted), we are effectively measuring topological charge along a longitudinal loop $\gamma \subset T$ in a torus boundary component of a topological space-time fluid. A cavity N bounded by T arises as the stream of probes B annihilates the topological fluid along the interferometry loop, as discussed in Section 3.5. The measurement outcome effectively replaces the deleted solid torus and boundary (N, T) by a new one (N', T') with meridian (T') glued to longitude (T). The new solid torus N', within this effective description, enforces the measured charge a. To do this it contains a Wilson loop labeled by topological charge a at its core.

Given a TQFT, one should think of a given 3-manifold M with boundary as a family of tensors that depend on how its boundary is divided into pieces. In the next section, we see that this is already a rich discussion when the TQFT is the Ising theory, M is a solid torus and ∂M is divided into two annuli, but *partitioned* in a variety of ways. For the Ising TQFT (with connected complement C), the effect of interferometric measurement is merely a Dehn surgery (with ω_a Wilson loops having $a = I$ or ψ, depending on measurement outcome) effecting a tensor contraction with the observed state.

4.2 TQFTs: A Fixed 3-Manifold Yields Many Tensors According to its Boundary Decomposition

The 3-manifold M plays the role of the tensor $\mathcal{T}$, but its valence is unspecified until the (2-manifold) boundary of M is dissected into pieces. These pieces may be closed or themselves have a 1-manifold boundary, which specifies the index set for the tensor. The axioms for TQFTs strongly restrict which tensors arise as the boundary decomposition of M is varied. For a key example, take M to be a solid torus $S^1 \times D^2$ and the Ising TQFT (see Section 3.6 for a summary of the

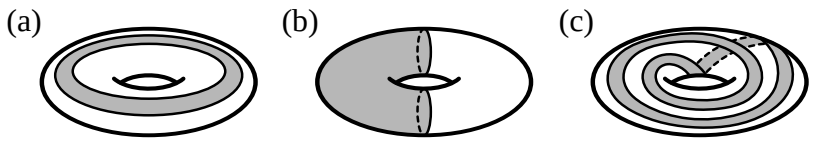

Fig. 4.2. Three different decompositions of the 2D torus boundary of a 3D solid torus. In each of these examples, the boundary torus is partitioned into two annuli, which are colored white and grey, respectively.

Ising TQFT rules). Decomposing the 2D torus boundary ∂M into annuli A and B ($\partial M = A \cup B$) as shown in Fig. 4.2 yields three different matrices (2-tensors), with indices corresponding to the I, σ, and ψ topological charge basis along the two loops (1-manifolds) of $A \cap B$. These boundary partitions will be useful, so we sketch how the calculations are done for the examples in Fig. 4.2.

For the boundary partition in Fig. 4.2(a), the result is axiomatic: products correspond to identity morphisms. The identity operator "glues up" to become the vector (1-index tensor)

$$v_l = \begin{pmatrix} \frac{d_I}{\mathcal{D}} \\ \frac{d_\sigma}{\mathcal{D}} \\ \frac{d_\psi}{\mathcal{D}} \end{pmatrix} = \begin{pmatrix} \frac{1}{2} \\ \frac{\sqrt{2}}{2} \\ \frac{1}{2} \end{pmatrix} \tag{4.2}$$

in the vector space $V_l(T)$ corresponding to the longitudinal basis. The corresponding operator $\mathcal{O}_l = \mathbb{I}$ is obtained by placing the entries of the vector on the diagonal of the matrix and dividing by $S_{I,a} = \frac{d_a}{\mathcal{D}}$ to obtain the proper normalization, i.e.

$$[\mathcal{O}]_{a,b} = \frac{[v]_a}{S_{I,a}} \delta_{a,b}. \tag{4.3}$$

The result for the boundary partition in Fig. 4.2(b) can be obtained from (a) by applying the modular S-transformation

$$S = \frac{1}{2} \begin{bmatrix} 1 & \sqrt{2} & 1 \\ \sqrt{2} & 0 & -\sqrt{2} \\ 1 & -\sqrt{2} & 1 \end{bmatrix}, \tag{4.4}$$

which transforms between the longitudinal and meridional bases. In this way, we obtain

$$v_m = S(v_l) = \begin{pmatrix} 1 \\ 0 \\ 0 \end{pmatrix}. \tag{4.5}$$

The corresponding operator is

$$\mathcal{O}_m = \begin{bmatrix} 2\ 0\ 0 \\ 0\ 0\ 0 \\ 0\ 0\ 0 \end{bmatrix}. \tag{4.6}$$

Finally, to compute the result for Fig. 4.2(c), we note that

$$B = ST^2S^{-1} = \begin{bmatrix} \frac{1+\omega}{2} & 0 & \frac{1-\omega}{2} \\ 0 & 1 & 0 \\ \frac{1-\omega}{2} & 0 & \frac{1+\omega}{2} \end{bmatrix}, \tag{4.7}$$

with $\omega = e^{i2\pi/8}$, is the modular transformation sending (b) to (c), where

$$T = \begin{bmatrix} 1 & 0 & 0 \\ 0 & e^{i\frac{2\pi}{16}} & 0 \\ 0 & 0 & -1 \end{bmatrix} \tag{4.8}$$

is the modular Dehn twist transformation, which cuts open the torus along the meridian and glues it back together with a 2π twist. Then, in this twisted basis (t), the vector for Fig. 4.2(c) is

$$v_t = B(v_m) = \begin{pmatrix} \frac{1+\omega}{2} \\ 0 \\ \frac{1-\omega}{2} \end{pmatrix}. \tag{4.9}$$

The corresponding operator is

$$\mathcal{O}_t = \begin{bmatrix} 1+\omega & 0 & 0 \\ 0 & 0 & 0 \\ 0 & 0 & 1-\omega \end{bmatrix}, \tag{4.10}$$

where, as mentioned, we divided entries by $S_{I,a} = \frac{d_a}{\mathcal{D}}$ to obtain the proper normalization.

We record also the vector and operator associated with a case (c′), which is the same boundary data as case (c), but with the solid torus containing a ψ-charge Wilson loop running along its core. In case (c′), we should now apply the above to

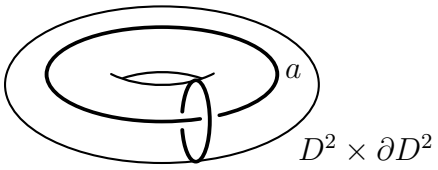

Fig. 4.3. Glue along the torus $T^2 = \partial D^2 \times \partial D^2$, respecting the framing of γ. Here, $a = I$ or ψ, the measured charge on curve γ.

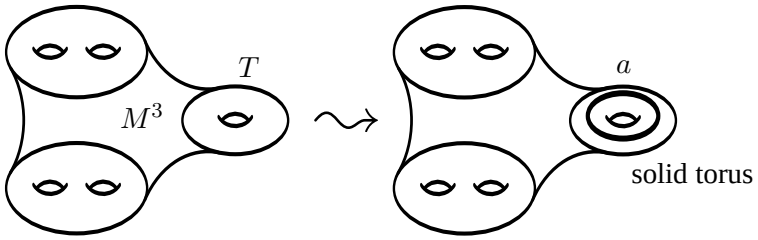

(a) (b)

Fig. 4.4. Measurement with outcome observing topological charge a along the curve γ. Note the analogy to Fig. 4.1.

the vector $v'_m = (0, 0, 1)^T$ corresponding to meridinal charge ψ. This gives

$$v_t = B(v'_m) = \begin{pmatrix} \frac{1-\omega}{2} \\ 0 \\ \frac{1+\omega}{2} \end{pmatrix}. \tag{4.11}$$

Thus, the corresponding operator is

$$\mathcal{O}_t = \begin{bmatrix} 1-\omega & 0 & 0 \\ 0 & 0 & 0 \\ 0 & 0 & 1+\omega \end{bmatrix}. \tag{4.12}$$

Gluing a 3 dimensional solid torus $D^2 \times S^1 = D^2 \times \partial D^2$ is the TQFT equivalent of tracing (summing over a repeated index). In our application, $D^2 \times \partial D^2$ is a solid torus of space-time topological fluid glued into the cavity created by removing a solid torus ($D^2 \times \partial D^2$) neighborhood of the interferometry loop γ. The gluing should respect the framing on γ.

The topological charge a line at the core of the replacement solid torus is precisely the measurement outcome $a = I$ or ψ. (If the measured topological charge value is trivial I, the solid torus has no Wilson line.) Up to an overall scalar, which has no physical significance, measuring charge a along the curve γ is equivalent to

deleting a $D^2 \times \partial D^2$ neighborhood of γ and re-gluing $D^2 \times \partial D^2$ with $* \times \partial D^2$ matching the first normal frame vector to γ, $* \in \partial D^2$, and $0 \times \partial D^2$ being a Wilson loop of charge a. Thus a measurement of $a = I$ or ψ Dehn fills a new solid torus near γ with a Wilson loop of charge a at its core.

4.3 Effect of Twisting: The $\pi/8$-phase gate

In Section 4.2, we calculated the operator $\mathcal{O}_t$ associated to a solid torus with $(1, -2)$-twisted boundary, as shown in Fig. 4.2(c), containing an I or ψ Wilson loop. In the longitudinal basis, restricted to topological charge values I and ψ, this was given by

$$\mathcal{O}_t = \begin{bmatrix} 1+\omega & 0 \\ 0 & 1-\omega \end{bmatrix} \quad \text{or} \quad \begin{bmatrix} 1-\omega & 0 \\ 0 & 1+\omega \end{bmatrix}. \tag{4.13}$$

according to whether the Wilson loop has charge I or ψ. This operator, together with Ising anyon braiding transformations and standard (untwisted) interferometry measurements, allows one to generate $\pi/8$-phase gates

$$R_{\frac{\pi}{4}} = \begin{bmatrix} 1 & 0 \\ 0 & e^{i\pi/4} \end{bmatrix}. \tag{4.14}$$

In particular, applying $\mathcal{O}_t$ to the state $\frac{1}{\sqrt{2}}(|0\rangle + |1\rangle) = H|0\rangle$, where the Hadamard operator

$$H = \frac{1}{\sqrt{2}} \begin{bmatrix} 1 & 1 \\ 1 & -1 \end{bmatrix} \tag{4.15}$$

can be obtained as a braiding transformation, generates the "magic state"

$$\left|\mathcal{B}_{-\frac{\pi}{4}}\right\rangle = H R_{\frac{\pi}{4}} H \,|0\rangle = \cos(\pi/8)\,|0\rangle - i\sin(\pi/8)\,|1\rangle \tag{4.16}$$

(up to an overall scalar that is removed by normalization) or

$$\left|\mathcal{B}_{\frac{3\pi}{4}}\right\rangle = \sigma^x H R_{\frac{\pi}{4}} H \,|0\rangle = \sin(\pi/8)\,|0\rangle + i\cos(\pi/8)\,|1\rangle\,, \tag{4.17}$$

depending on whether one uses the I or ψ operator $\mathcal{O}_t$. Using Ising braiding gates and measurements, any magic state (such as these) can be transformed into $\pi/8$-phase gates.

In the untwisted context, the measurement imposes one of the two projections, in the basis of topological charge I or ψ enclosed in the untwisted interferometry loop, given by

$$\Pi_0 = \begin{bmatrix} 1 & 0 \\ 0 & 0 \end{bmatrix}, \tag{4.18}$$

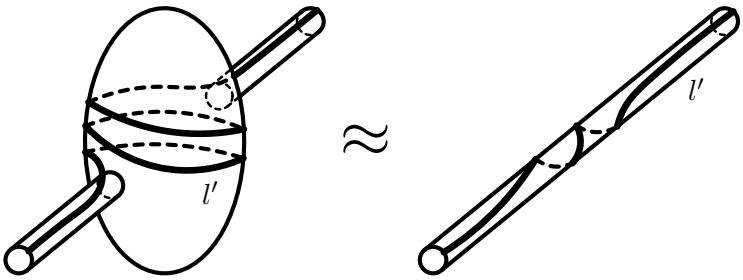

Fig. 4.5. Twisted interferometry loop l' near vacuum island.

if charge I is observed and

$$\Pi_1 = \begin{bmatrix} 0 & 0 \\ 0 & 1 \end{bmatrix}, \tag{4.19}$$

if charge ψ is observed. One might naïvely expect the twisted interferometer to generate conjugates of Π_0 and Π_1, however, this is not correct because the matrices obtained have rank 2. Since no charge lines enter or leave the twisted interferometer (and we always assume there are no mobile charges) the twisted interferometry operator $\mathcal{O}_t$ must be diagonal in the I, ψ basis of topological charge [which is a consistency check on Eq. (4.13)].

The relation between the twisted interferometric path and the boundary conditions of Fig. 4.2(c) is show in Figs. 4.5 and 4.6. In Fig. 4.5, the two extra trips around the island or along the twisted track mean that measurement is applied along a topologically twisted $(1, -2)$ loop, which is related to the spatial perimeter of the interferometer l by a change of coordinates described by $B = S^{-1}T^2S$. Referring to Figs. 4.5 and 4.6, we see that the two changes of coordinates described in Section 4.2 computes $\mathcal{O}_t$, in the case of the two measurement outcomes I or ψ.

Suppose l is the outer boundary of a standard Ising qubit encoded in the I and ψ fusion channels of σ anyons. Running a generically tuned doubly twisted interferometer (with σ probe quasiparticles that are assumed to have negligible probe-probe interaction) around l (equivalent to γ in Fig. 4.6 via Fig. 4.5) asymptotically realizes the $\mathcal{O}_t$ operator (up to exponentially suppressed corrections), which can be used to implement a $\pi/8$-phase gate.

5 Protocol for Direct Implementation of $\pi/8$-Phase Gate

We now exhibit a topological protocol for using twisted interferometry to directly generate a $\pi/8$-phase gate, rather than by generating magic states (which are subsequently used to produce a $\pi/8$-phase gate). In comparison, this protocol has the advantage of being more efficient and not utilizing entangling gates. However, it requires that the twisted interferometry operation have sufficiently small errors,

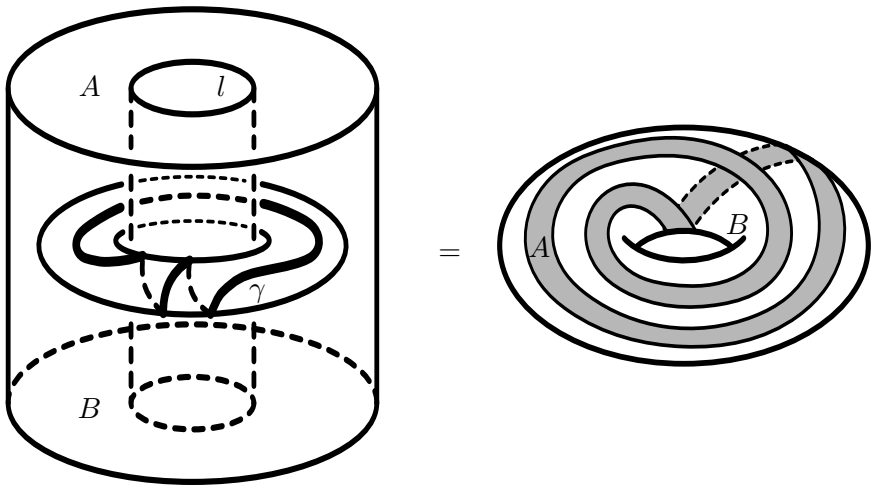

Fig. 4.6. A change of coordinates using Dehn twists equates the solid torus describing the region of space-time in which the twisted interferometry takes place (left) with the solid torus with the previously analyzed boundary partition (right). The anyons being measured are contained within the missing core, i.e. are enclosed in the spatial plane (a time slice) by the loop l. The top annular boundary region A on the left maps to the shaded twisted band A on the surface of the solid torus on the right; the bottom annular boundary region B on the left maps to the white twisted band B on the surface of the solid torus on the right; the inner and outer vertical boundaries of the solid on the left map to the two boundaries (black lines) separating the regions A and B on the surface of the solid torus on the right. Measuring l' Dehn fills a solid torus on the right, so that l' bounds a disk or disk with ψ anyon. If the measurement outcome is $a = I$ or ψ, there is a Wilson loop of charge a at the core of the solid torus.

whereas the magic state generation protocol allows one to apply a high error threshold error-correction protocol, known as magic state distillation [46], if the twisted interferometry operation is not sufficiently free of error. The protocol described here, summarized in Fig. 5.1, exhibits the roots of twisted interferometry in surfaces of positive genus. This protocol can be viewed as another translation of the $\pi/8$-phase gate protocol of Ref. [39], which was developed in the series of papers [40,41,42], in this case utilizing twisted interferometry.

In Fig. 5.1, the $t = 0$ slice depicts a topological qubit partially encoded in two anti-dots, i.e. S^1 boundaries between the (spatial) system and vacuum. Each of the anti-dots/boundaries carries topological charge σ and the I and ψ fusion channels of this pair comprise the qubit basis states. The first event (as time increases) is the creation of a new anti-dot (the local minima), which carries trivial topological charge I. At the saddle point, this anti-dot splits into two anti-dots (two S^1 boundaries between the system and vacuum), each of which carries topological charge σ. This charge distribution is not random, so it must be controlled using appropriately tuned potential wells and/or local measurements of the topological charge on the anti-dots. The third object occurring in Fig. 5.1, is the twisted interferometric loop γ. By Section 4, γ will carry an ω_a, depending on the twisted interferometry measurement outcome $a = I$ or ψ. In other words, this indicates which of the two

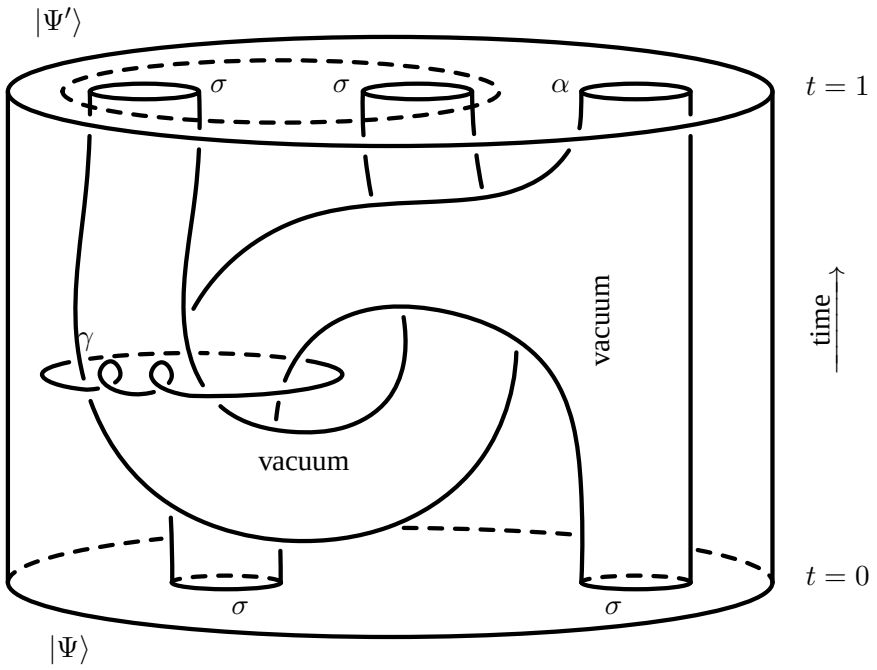

Fig. 5.1. Summary of $\pi/8$-phase gate protocol.

types of Dehn surgery has been done on γ. The fourth event is a fusion of the pair of σ charged anti-dots of the original qubit into a single anti-dot with topological charge $\alpha = I$ or ψ, which are equal probability outcomes of the fusion. The fifth event is a topological charge measurement of the charge α, which can be measured by ordinary quasiparticle interferometry or a local energetic measurement. In the case when the measurement outcome is $\alpha = \psi$, an addition final step, not shown in Fig. 5.1 to avoid excessive clutter, is needed, wherein the anti-dot/boundary carrying charge $\alpha = \psi$ is fused/merged with one of the final anti-dots/boundaries carrying charge σ. This is necessary for the final system topological charge configuration to match the initial configuration. In other words, the final qubit state is (partially) encoded by the two charge σ boundaries (contained within the dashed circle) on the $t = 1$ surface, but, if $\alpha = \psi$, then this final step is necessary for it to be encoded in the same manner as it was at $t = 0$.

The initial state $|\Psi\rangle$ at $t = 0$ transforms into the final state $|\Psi'\rangle = U(a, \alpha)|\Psi\rangle$ at time $t = 1$, where the operator $U(a, \alpha)$ depends on the twisted interferometry measurement outcome $a = I$ or ψ (i.e. the label ω_a on curve γ) and the measurement outcome of the topological charge α. Using standard techniques of quantum topology, we will verify that the (single-qubit) operator $U(a, \alpha)$ acting on this topological qubit is given (up to insignificant overall phases) by

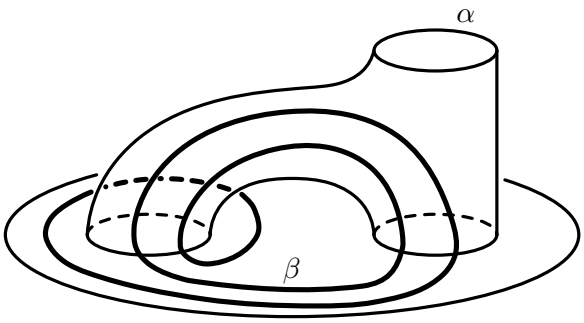

Fig. 5.2. Cutting the (boundary) surface along β.

$$U(I,I) = U(\psi,I) = \begin{bmatrix} 1 & 0 \\ 0 & e^{-i\pi/4} \end{bmatrix} = R_{-\frac{\pi}{4}} = R_{-\frac{\pi}{2}} R_{\frac{\pi}{4}} \tag{5.1}$$

$$U(I,\psi) = U(\psi,\psi) = \begin{bmatrix} 1 & 0 \\ 0 & e^{-i3\pi/4} \end{bmatrix} = R_{-\frac{3\pi}{4}} = R_{-\pi} R_{\frac{\pi}{4}} \tag{5.2}$$

Clearly, these are all related to the $\pi/8$-phase gate $R_{\frac{\pi}{4}}$ by a single-qubit Clifford gate, which may be generated using braiding transformations of Ising σ quasiparticles.

As seen in Refs. [40,41,42], the $-\pi/8$-phase gate $R_{-\frac{\pi}{4}}$ is obtained, between the geometrically distinct initial and final "marked pants," by cutting the surface open along β in Fig. 5.2 if topological charge $\alpha = I$, and its inverse $R_{\frac{\pi}{4}}$ (the $\pi/8$-phase gate) if $\alpha = \psi$. Thickening the surface in Fig. 5.2 results in Fig. 5.3. Now the framed curve γ in Fig. 5.1 is precisely the surgery required to send β to the meridian μ labeled in Fig. 5.3. In both cases, the twisted interferometry measurement outcome $a = I$ effects ordinary framed surgery, while measuring $a = \psi$ effects a variant in which the core of the replacement solid torus carries a ψ-charge. The matrices in Eqs. (5.1)-(5.2) give the precise gates $U(a,\alpha)$ executed according to the two outcomes a and α. Since the original qubit has σ charges on its internal punctures, there will also be a σ-charge on β (see Fig. 5.2), but compared to the original qubit at time $t = 0$, the relative phase between the two fusion channels I and ψ is now changed.

The loop β' in Fig. 5.3 is simply a copy of β transported across the product structure, i.e. through the topologically trivial $(2+1)$D spacetime bulk from one boundary surface to another. A -1 Dehn twist on the loop γ' throws β' to the meridian μ. Thus, Dehn surgery on a torus in the bulk parallel to γ', with a -1 additional twist in its framing compared to the normal framing of γ' inherited from the boundary of the bulk, endows the bulk with a new product structure in which β is connected by a cylinder to the meridian μ. The curve γ, as drawn in Fig. 5.1, is this additionally -1 framed bulk loop isotopic to γ'. Thus, twisted interferometry with outcome $a = I$, in a sense, "teleports" the state from the non-time-slice qubit defined by cutting the surface of Fig. 5.2 along β to the "untwisted" time-slice qubit defined by the top

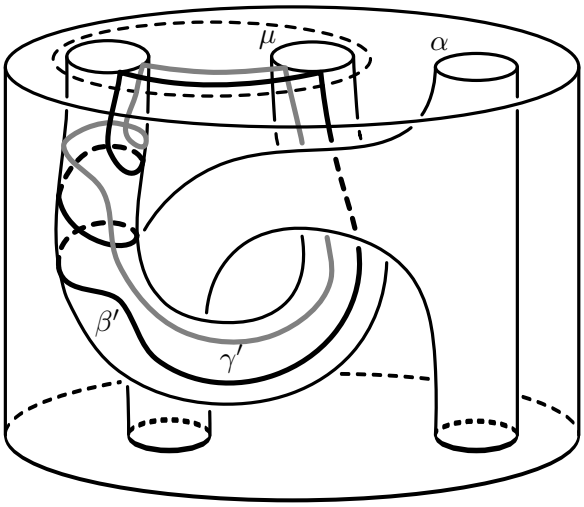

Fig. 5.3. Thickening the surface from Fig. 5.2.

surface of Fig. 5.3.

It remains to compute the effect of this protocol if the twisted interferometry measurement outcome is $a = \psi$. (Note: $a = \sigma$ is not a possible outcome as the charge along $\gamma = l' = (1, -2)$ is obtained from the charge along l, which is initially in the $\{I, \psi\}$ sector, by applying the matrix $B = ST^2S^{-1}$, which does not mix the $\{I, \psi\}$ sector and the σ sector of the charge along l.) The effect of outcome $a = \psi$ will be a Wilson loop γ'' of charge ψ parallel to γ' (in the bulk) with no additional twist in its framing.

Using the diagrammatic rules of UMTCs, we see that the effect of the protocol on the topological qubit basis states $q = I$ and ψ is given by

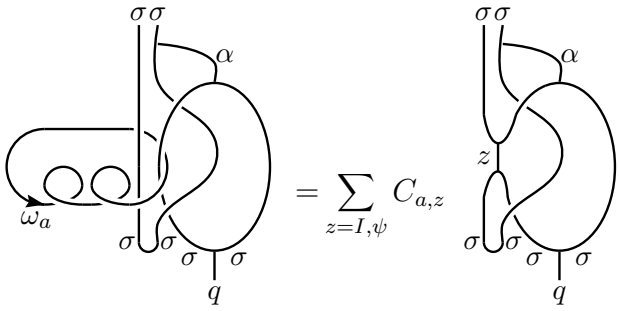

$$= \sum_{z=I,\psi} C_{a,z}$$

$$= \sum_{z=I,\psi} C_{a,z}(-1)^{zq+z\alpha+z+\alpha q} e^{i\pi/8} R_\sigma^{\alpha\sigma} \left[R_q^{\sigma\sigma}\right]^{-1}$$

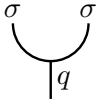

$$= [U(a,\alpha)]_{q,q}$$

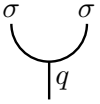

(5.3)

where $C_{I,I} = C_{\psi,\psi} = \cos(\pi/8)$ and $C_{I,\psi} = C_{\psi,I} = i\sin(\pi/8)$ are the coefficients resulting from the twisted interferometry with $(-2, 0)$ twisting and outcome a. When the topological charge values I and ψ are written in the exponent, they are taken to mean 0 and 1, respectively. The coefficients $[U(a, \alpha)]_{q,q}$ in the final line are the diagonal elements of the unitary matrices $U(a, \alpha)$ (up to unimportant overall phases, i.e. phases that are independent of q) given in Eqs. (5.1) and (5.2). It is clear from the diagrams that the off-diagonal elements of the operators generated by this protocol must vanish, by conservation of topological charge.

Acknowledgements

We thank R. Lutchyn, C. Nayak, K. Shtengel, and J. Slingerland for illuminating discussions. P. B. and M. F. thank the Aspen Center for Physics for hospitality and support under the NSF Grant No. 1066293.

References

[1] P. H. Bonderson, Non-Abelian Anyons and Interferometry, Ph.D. thesis, California Institute of Technology (2007).

[2] P. Bonderson, K. Shtengel, J. K. Slingerland, Interferometry of non-Abelian Anyons, Annals Phys. 323 (2008) 2709, arXiv:0707.4206.

[3] A. Y. Kitaev, Fault-tolerant quantum computation by anyons, Annals Phys. 303 (2003) 2, quant-ph/9707021.

[4] M. H. Freedman, P/NP, and the quantum field computer, Proc. Natl. Acad. Sci. USA 95 (1998) 98.

[5] J. Preskill, Fault-tolerant quantum computation, in: H.-K. Lo, S. Popescu, T. P. Spiller (Eds.), Introduction to Quantum Computation, World Scientific, 1998.

[6] M. H. Freedman, M. J. Larsen, Z. Wang, A modular functor which is universal for quantum computation, Commun. Math. Phys. 227 (2002) 605, quant-ph/0001108.

[7] M. H. Freedman, M. J. Larsen, Z. Wang, The two-eigenvalue problem and density of Jones representation of braid groups, Commun. Math. Phys. 228 (2002) 177, math/0103200.

[8] M. H. Freedman, A. Kitaev, M. J. Larsen, Z. Wang, Topological quantum computation, Bull. Amer. Math. Soc. 40 (2003) 31, quant-ph/0101025.

[9] C. Nayak, S. H. Simon, A. Stern, M. Freedman, S. Das Sarma, Non-abelian anyons and topological quantum computation, Rev. Mod. Phys. 80 (2008) 1083, arXiv:0707.1889.

[10] P. Bonderson, M. Freedman, C. Nayak, Measurement-Only Topological Quantum Computation, Phys. Rev. Lett. 101 (2008) 010501, arXiv:0802.0279.

[11] P. Bonderson, M. Freedman, C. Nayak, Measurement-Only Topological Quantum Computation via Anyonic Interferometry, Annals Phys. 324 (2009) 787, arXiv:0808.1933.

[12] S. Bravyi, A. Kitaev, Fermionic quantum computation, Annals Phys. 298 (2002) 210, quant-ph/0003137.

[13] S. Bravyi, Universal quantum computation with the $\nu = 5/2$ fractional quantum Hall state, Phys. Rev. A 73 (2006) 042313, quant-ph/0511178.

[14] P. Bonderson, unpublished.

[15] C. Levaillant, B. Bauer, M. Freedman, Z. Wang, P. Bonderson, Universal gates via fusion and measurement operations on $\mathrm{SU}(2)_4$ anyons, Phys. Rev. A 92 (2015) 012301, arXiv:1504.02098.

[16] C. de C. Chamon, D. E. Freed, S. A. Kivelson, S. L. Sondhi, X. G. Wen, Two point-contact interferometer for quantum Hall systems, Phys. Rev. B 55 (1997) 2331, cond-mat/9607195.

[17] E. Fradkin, C. Nayak, A. Tsvelik, F. Wilczek, A Chern-Simons effective field theory for the Pfaffian quantum Hall state, Nucl. Phys. B 516 (1998) 704, cond-mat/9711087.

[18] S. Das Sarma, M. Freedman, C. Nayak, Topologically protected qubits from a possible non-Abelian fractional quantum Hall state, Phys. Rev. Lett. 94 (2005) 166802, cond-mat/0412343.

[19] A. Stern, B. I. Halperin, Proposed experiments to probe the non-abelian $\nu = 5/2$ quantum Hall state, Phys. Rev. Lett. 96 (2006) 016802, cond-mat/0508447.

[20] P. Bonderson, A. Kitaev, K. Shtengel, Detecting non-Abelian statistics in the $\nu = 5/2$ fractional quantum Hall state, Phys. Rev. Lett. 96 (2006) 016803, cond-mat/0508616.

[21] P. Bonderson, K. Shtengel, J. K. Slingerland, Probing non-Abelian statistics with quasiparticle interferometry, Phys. Rev. Lett. 97 (2006) 016401, cond-mat/0601242.

[22] L. Fidkowski, Double point contact in the k=3 Read–Rezayi state, arXiv:0704.3291.

[23] E. Ardonne, E.-A. Kim, Non-Abelian statistics in the interference noise of the Moore-Read quantum Hall state, J. Stat. Mech. 4 (2008) L04001, arXiv:0705.2902.

[24] W. Bishara, C. Nayak, Edge states and interferometers in the pfaffian and anti-pfaffian states, Phys. Rev. B 77 (2008) 165302, arXiv:0708.2704.

[25] W. Bishara, P. Bonderson, C. Nayak, K. Shtengel, J. K. Slingerland, The non-Abelian Interferometer, Phys. Rev. B 80 (2009) 155303, arXiv:0903.3108.

[26] A. R. Akhmerov, J. Nilsson, C. W. J. Beenakker, Electrically Detected Interferometry of Majorana Fermions in a Topological Insulator, Phys. Rev. Lett. 102 (2009) 216404, arXiv:0903.2196.

[27] L. Fu, C. L. Kane, Probing Neutral Majorana Fermion Edge Modes with Charge Transport, Phys. Rev. Lett. 102 (2009) 216403, arXiv:0903.2427.

[28] P. Bonderson, R. M. Lutchyn, Topological quantum buses: coherent quantum information transfer between topological and conventional qubits, Phys. Rev. Lett. 106 (2011) 130505, arXiv:1011.1784.

[29] E. Grosfeld, A. Stern, Observing Majorana bound states of Josephson vortices in topological superconductors, Proc. Natl. Acad. Sci. USA 108 (2011) 11810, arXiv:1012.2492.

[30] F. E. Camino, W. Zhou, V. J. Goldman, Realization of a Laughlin quasiparticle interferometer: Observation of fractional statistics, Phys. Rev. B 72 (2005) 075342, cond-mat/0502406.

[31] R. L. Willett, L. N. Pfeiffer, K. W. West, Measurement of filling factor 5/2 quasiparticle interference with observation of charge e/4 and e/2 period oscillations, Proc. Natl. Acad. Sci. 106 (2009) 8853, arXiv:0807.0221.

[32] R. L. Willett, L. N. Pfeiffer, K. W. West, Alternation and interchange of e/4 and e/2 period interference oscillations as evidence for filling factor 5/2 non-abelian quasiparticles, arXiv:0911.0345.

[33] D. T. McClure, W. Chang, C. M. Marcus, L. N. Pfeiffer, K. W. West, Fabry-perot interferometry with fractional charges, Phys. Rev. Lett. 108 (2012) 256804, arXiv:1112.0538.

[34] S. An, P. Jiang, H. Choi, W. Kang, S. H. Simon, L. N. Pfeiffer, K. W. West, K. W. Baldwin, Braiding of abelian and non-abelian anyons in the fractional quantum hall effect, arXiv:1112.3400.

[35] R. L. Willett, L. N. Pfeiffer, K. W. West, Magnetic field induced resistance properties at filling factor 5/2 consistent with non-Abelian e/4 quasiparticles in multiple sized interferometers, arXiv:1204.1993.

[36] R. L. Willett, C. Nayak, K. Shtengel, L. N. Pfeiffer, K. W. West, Magnetic field-tuned Aharonov-Bohm oscillations and evidence for non-Abelian anyons at $\nu = 5/2$, arXiv:1204.1993.

[37] D. Gottesman, The heisenberg representation of quantum computers, quant-ph/9807006.

[38] P. O. Boykin, T. Mor, M. Pulver, V. Roychowdhury, F. Vatan, On universal and fault-tolerant quantum computing, in: Proc. 40th FOCS, Society Press, 1999, p. 486.

[39] S. B. Bravyi, A. Y. Kitaev, Quantum invariants of 3-manifolds and quantum computation (2000), unpublished.

[40] M. Freedman, C. Nayak, K. Walker, Towards universal topological quantum computation in the $\nu = 5/2$ fractional quantum Hall state, Phys. Rev. B 73 (2006) 245307, cond-mat/0512066.

[41] M. Freedman, C. Nayak, K. Walker, Tilted interferometry realizes universal quantum computation in the Ising TQFT without overpasses, cond-mat/0512072.

[42] P. Bonderson, S. Das Sarma, M. Freedman, C. Nayak, A blueprint for a topologically fault-tolerant quantum computer, arXiv:1003.2856.

[43] P. Bonderson, K. Shtengel, J. K. Slingerland, Decoherence of anyonic charge in interferometry measurements, Phys. Rev. Lett. 98 (2007) 070401, quant-ph/0608119.

[44] E. Witten, Quantum field theory and the Jones polynomial, Comm. Math. Phys. 121 (1989) 351.

[45] P. Bonderson, L. Fidkowski, M. Freedman, K. Walker, Twisted interferometry, arXiv:1306.2379.

[46] S. Bravyi, A. Kitaev, Universal quantum computation with ideal Clifford gates and noisy ancillas, Phys. Rev. A 71 (2005) 022316, quant-ph/0403025.